nature communications

Article

https://doi.org/10.1038/s41467-024-52688-6

Depth-dependent study of time-reversal symmetry-breaking in the kagome superconductor AV_3Sb_5

Received: 23 June 2024

Accepted: 16 September 2024

J. N. Graham[1,11], C. Mielke III[1,11], D. Das[1,11], T. Morresi[2], V. Sazgari[1], A. Suter[1], T. Prokscha[1], H. Deng[3], R. Khasanov[1], S. D. Wilson[4], A. C. Salinas[4], M. M. Martins[1], Y. Zhong[5], K. Okazaki[5], Z. Wang[6], M. Z. Hasan[7], M. H. Fischer[8], T. Neupert[8], J. -X. Yin[3], S. Sanna[9], H. Luetkens[1], Z. Salman[1], P. Bonfà[10] ✉ & Z. Guguchia[1] ✉

The breaking of time-reversal symmetry (TRS) in the normal state of kagome superconductors AV_3Sb_5 stands out as a significant feature, but its tunability is unexplored. Using low-energy muon spin rotation and local field numerical analysis, we study TRS breaking as a function of depth in single crystals of RbV_3Sb_5 (with charge order) and $Cs(V_{0.86}Ta_{0.14})_3Sb_5$ (without charge order). In the bulk of RbV_3Sb_5 (>33 nm from the surface), we observed an increase in the internal magnetic field width in the charge-ordered state. Near the surface (<33 nm), the muon spin relaxation rate is significantly enhanced and this effect commences at temperatures significantly higher than the onset of charge order. In contrast, no similar field width enhancement was detected in $Cs(V_{0.86}Ta_{0.14})_3Sb_5$, either in the bulk or near the surface. These observations indicate a strong connection between charge order and TRS breaking and suggest that TRS breaking can occur prior to long-range charge order.

The concept of chiral (TRS breaking) charge order is a fascinating aspect of modern condensed matter physics, reflecting a state where electron arrangements break mirror symmetry, akin to left-handed and right-handed twists. This chiral charge ordering can lead to unconventional electronic properties[1–28], and host exotic quasi-particles, potentially useful for quantum computing and novel electronic devices due to its influence on electronic band structures and interactions.

The AV_3Sb_5 kagome superconductors represent a unique and ideal platform known for hosting charge orders that possibly break TRS[11–13,15,16,29–34]. This phenomenon of high-temperature TRS breaking charge order is exceedingly rare. It offers a profound analogy to pivotal theoretical models in physics: the Haldane model[35] for the honeycomb lattice and the Varma model[36] for the square lattice. The evidence for TRS breaking in these materials primarily comes from zero-field and high-field muon spin rotation (μSR) measurements. μSR, recognized for its exceptional sensitivity to magnetic phenomena[15,37–40], has provided indications of TRS breaking in the charge ordered state of all three variants of AV_3Sb_5; KV_3Sb_5[12], RbV_3Sb_5[13], and CsV_3Sb_5[16]. This

---

[1] Laboratory for Muon Spin Spectroscopy, PSI Center for Neutron and Muon Sciences, Paul Scherrer Institut, CH-5232 Villigen PSI, Switzerland. [2] European Centre for Theoretical Studies in Nuclear Physics and Related Areas (ECT*), Fondazione Bruno Kessler, Trento, Italy. [3] Department of Physics, Southern University of Science and Technology, Shenzhen, Guangdong, China. [4] Materials Department, Materials Research Laboratory, and California NanoSystems Institute, University of California Santa Barbara, Santa Barbara, USA. [5] Institute for Solid States Physics, The University of Tokyo, Kashiwa, Japan. [6] Centre for Quantum Physics, Key Laboratory of Advanced Optoelectronic Quantum Architecture and Measurement (MOE), School of Physics, Beijing Institute of Technology, Beijing, China. [7] Laboratory for Topological Quantum Matter and Advanced Spectroscopy (B7), Department of Physics, Princeton University, Princeton, USA. [8] Physik-Institut, Universität Zürich, Zürich, Switzerland. [9] Dipartimento di Fisica e Astronomia "A. Righi", Universitá di Bologna, Bologna, Italy. [10] Dipartimento di Scienze Matematiche, Fisiche e Informatiche, Università di Parma, Parma, Italy. [11] These authors contributed equally: J. N. Graham, C. Mielke III, D. Das. ✉ e-mail: pietro.bonfa@posteo.net; zurab.guguchia@psi.ch

uniformity across different compositions suggests that the nature of this symmetry breaking is intrinsic to Kagome superconductors in general.

In addition to the increase of the internal magnetic fields in the TRS breaking state by μSR, other manifestations of unconventional charge order in these materials have been observed. Notably, these include the giant anomalous Hall effect[24,25] detected through transport measurements. Furthermore, a field-tunable chirality switch effect[11,41–43] and the ability to control chiral transport[23] properties have been reported. These features point to the presence of chiral electronic states, which are sensitive to external magnetic fields. Kerr effect measurements regarding TRS breaking are contradictory; some indicate its presence[30], while others do not[44]. Among these various techniques, μSR stands out as arguably the most magnetically sensitive, providing a critical tool for detecting and understanding the subtle magnetic quantum phenomena occurring in these Kagome superconductors. The combination of high-temperature TRS breaking charge order and the unique set of properties in AV_3Sb_5 superconductors therefore not only challenge existing theoretical frameworks but also open up potential avenues for novel electronic applications[10].

Previous μSR experiments[12,13,15,16,29] have primarily focused on exploring the TRS breaking response within the bulk of AV_3Sb_5 superconductors. However, there is a notable gap in our understanding regarding the magnetic characteristics near the surfaces of these materials. The lack of understanding in this area is particularly crucial given the research on thin films[45], which show non-monotonic variations in charge ordering temperature as a function of thickness. Additionally, it is vital to comprehend the influence of the surface on the overall electronic and magnetic properties of the materials. Given this context, it becomes imperative to extend our investigations to probe the magnetism at the surface of AV_3Sb_5. Understanding surface magnetism is not only crucial for a comprehensive understanding of the material's magnetic properties, but also for unraveling the interplay between charge order and TRS breaking. Thus, a focused effort to explore and characterize the magnetic fingerprints at the surface of AV_3Sb_5 is essential to advance our knowledge in this area.

In this study, we utilize the unique low-energy muon spin rotation method[46,47], coupled with local field numerical analysis, to investigate the depth-dependent TRS breaking response in single crystals of RbV_3Sb_5 (which exhibits charge order) and $Cs(V_{0.86}Ta_{0.14})_3Sb_5$ (which does not exhibit charge order). In RbV_3Sb_5, we detect a notable fourfold enhancement of the zero-field muon spin relaxation rate near the crystals surface compared to the bulk. Calculations indicate that the observed increase in the relaxation rate is attributable to magnetism, rather than being a consequence of muon-induced structural distortions or a secondary effect due to structural changes stemming from charge order[48]. In $Cs(V_{0.86}Ta_{0.14})_3Sb_5$, which lacks charge order, there is no noticeable increase in the internal field width, both in the bulk and near the surface. These observations imply a strong connection between the TRS breaking response and the presence of charge order. This finding emphasizes the need for a microscopic understanding of why the surface offers more favorable conditions for the formation of novel magnetism.

Results and discussion

The AV_3Sb_5 structure comprises a Kagome lattice of V atoms interlaced with a hexagonal lattice of Sb atoms, crystallizing in the $P6/mmm$ space group (Fig. 1a, b). Scanning tunneling microscopy (STM) atomic topographic images of the Sb surface for RbV_3Sb_5 and $Cs(V_{0.86}Ta_{0.14})_3Sb_5$ single crystals are presented in Fig. 1c and d, respectively. The Fourier transform of the image for RbV_3Sb_5 (inset of Fig. 1c) reveals both 1 × 1 lattice Bragg peaks (blue circles) and 2 × 2 charge-order peaks (red circles). In contrast, the Fourier transform for $Cs(V_{0.86}Ta_{0.14})_3Sb_5$ displays only the Bragg peaks, indicating the absence of 2 × 2 ordering and thus charge order in this compound. The critical temperature for superconductivity and the superfluid density are significantly higher in $Cs(V_{0.86}Ta_{0.14})_3Sb_5$ compared to RbV_3Sb_5, as shown in the Supplementary Note 1 and the Supplementary Fig. 1. This enhancement is attributed to the complete suppression of charge order in the Ta-doped sample. Figure 1e illustrates a schematic of the zero-field (ZF) and transverse-field low-energy μSR setup. Various detectors placed around the sample track the incoming μ^+ and the outgoing e^+. We employed a muon beam with an adjustable energy range from $E = 1$ keV to 30 keV. Each E corresponds to a different muon implantation depth profile. This range of energies allows us to vary the implantation depths of the muons from a fraction of a nanometer up to 200 nm, therefore enabling us to conduct depth-dependent μSR studies (approximately $\bar{z}$ = 10–200 nm in depth). Figure 1f shows the muon implantation profile in $(Rb,Cs)V_3Sb_5$ for various implantation energies, simulated using the Monte Carlo algorithm TrimSP[46].

In Fig. 2a, we present high-statistics ZF-μSR spectra for RbV_3Sb_5, displayed as the polarization function $P_{ZF}(t) = A_{ZF}(t)/A_{ZF}(0)$. These measurements were taken both above and below the charge ordering temperature $T_{CO} \simeq 110$ K in the bulk of the material. A sizeable increase in the relaxation of the asymmetry observed at $T = 5$ K is accompanied by a gradual change from a Gaussian-like curve to a more exponential-like curve for $P(t)$ at early times. The ZF-μSR spectrum is well described using the Gaussian Kubo-Toyabe (GKT) depolarization function[49] multiplied by an exponential decay function, consistent with previous work[12]:

$$P_{ZF}^{\mathrm{GKT}}(t) = \left(\frac{1}{3} + \frac{2}{3}(1 - \Delta_{ZF}^2 t^2)\exp\left[-\frac{\Delta_{ZF}^2 t^2}{2}\right]\right)\exp(-\Gamma_{ZF} t) \qquad (1)$$

where Δ/γ_μ represents the width of the local field distribution, arising from nuclear moments and $\gamma_\mu/2\pi$ = 135.5 MHz/T is the muon gyromagnetic ratio. Γ_{ZF} is attributed to muon spin relaxation originating from electronic sources[12,15].

To obtain a quantitative understanding of the zero-field muon spin relaxation in RbV_3Sb_5, we utilized first-principles calculations to compute the muon polarization function, using Density Functional Theory (DFT) simulations within the DFT+μ approach[50]. The first principles prediction of $P(t)$ accounts for the interaction between the muon and the surrounding nuclear dipole moments. Additionally, the muon's impact on both the lattice and the electric field gradient at various nuclear sites was assessed. This is crucial since all isotopes in RbV_3Sb_5 undergo quadrupolar interactions. A comprehensive explanation of our methodology is available in the Supplementary Note 3 and Supplementary Figs. 3–9. Our analysis reveals a single stable muon site in RbV_3Sb_5, depicted in Fig. 2b. The muon's nearest neighbor is the in-plane Sb1 atom, followed by an Rb atom, with two hexagonal arrangements of out-of-plane Sb2 and V atoms from the kagome lattice as further neighbors. We then calculated the muon polarization function, $P(t)$, using Celio's approach[51], as implemented in the UNDI code[52]. This estimate does not include the uncertainties related to the ab initio estimates of atomic positions and electric field gradients. The calculated polarization closely matches experimental observations, albeit with a slightly faster depolarization. A perfect alignment with experimental data is achieved by minutely adjusting the muon's position, specifically a 0.03 Å shift from the nearest Sb atom. Notably, similar discrepancies have been observed in other DFT+μ studies[50,53]. At T~T_{CO}, the experimental and theoretical results align well, indicating that nuclear moments are predominantly responsible for the muon spin relaxation. However, the relaxation rates increase in the charge-ordered state indicating a deviation from static nuclear dipole-induced relaxation. Persisting with a nuclear-focused explanation for $P(t)$, the observed low-temperature variations imply significant shifts in the position or electronic environment of the muons two nearest neighbors, Sb1 and Rb, within the charge-ordered state. This is not mirrored

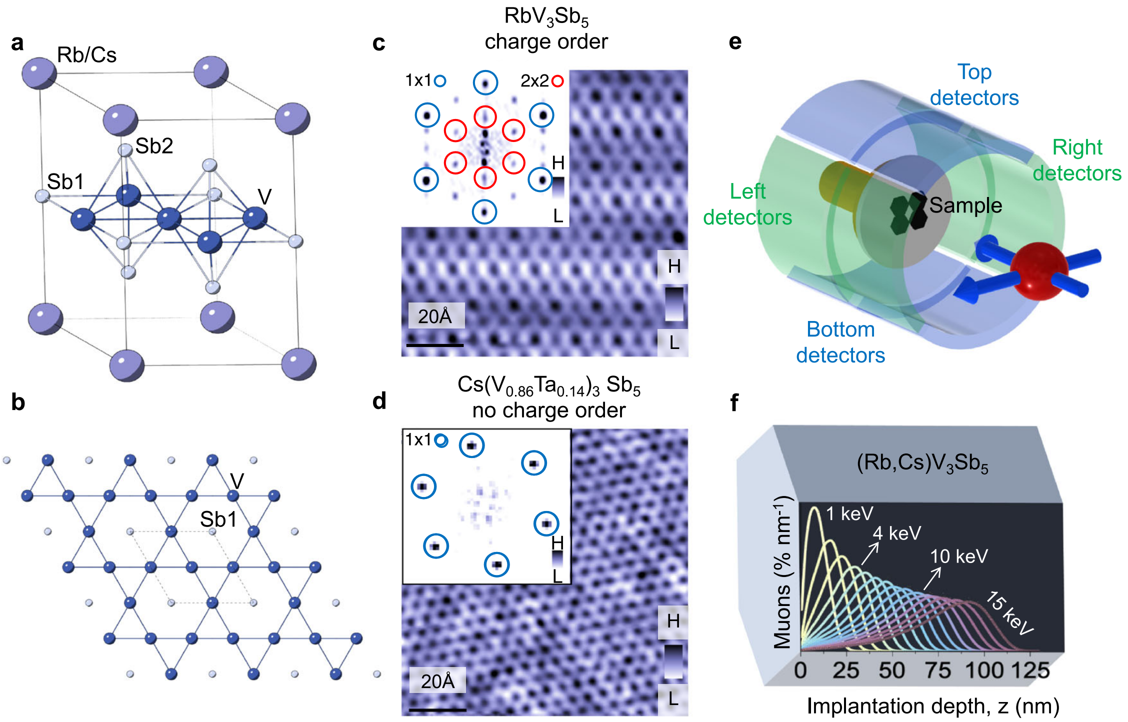

Fig. 1 | Atomic topographic images of AV_3Sb_5 and experimental setup. a The crystallographic structure of prototype compound AV_3Sb_5 (A = Rb or Cs). The V atoms form a kagome lattice intertwined with a hexagonal lattice of Sb atoms. The (Rb,Cs) atoms occupy the interstitial sites between the two parallel kagome planes. In (**b**) the vanadium kagome net has been emphasized, with the interpenetrating antimony lattice included to highlight the unit cell (see dashed lines). **c** Scanning tunneling microscopy of the Sb surface for RbV_3Sb_5. The inset is the Fourier transform of this image, displaying 1 × 1 lattice Bragg peaks (blue circles) and 2 × 2 charge-order peaks (red circles). **d** Atomic topographic image of Sb surface in Ta-doped $Cs(V_{0.86}Ta_{0.14})_3Sb_5$. The inset is the Fourier transform of this image, showing the absence of 2 × 2 ordering peaks, leaving only Bragg peaks. **e** Experimental LE-μSR setup with applied field vector B_{ext} perpendicular to the sample surface (i.e., along the c-axis of RbV_3Sb_5), and arrays of positron detectors used to count muon decay events. **f** Muon implantation profile of $(Rb,Cs)V_3Sb_5$ simulated for several implantation energies.

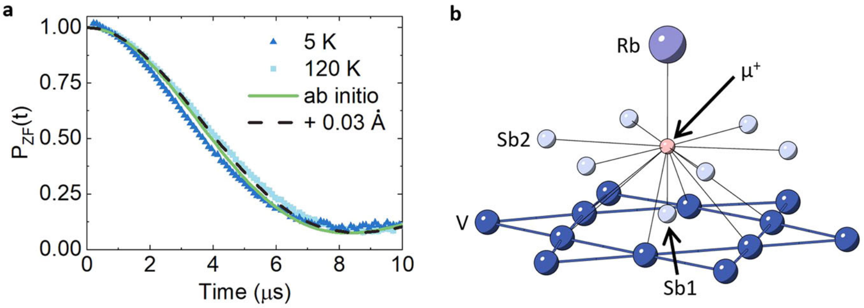

Fig. 2 | Muon stopping site and ab initio prediction in RbV_3Sb_5. a Zero-field μSR time spectra in the bulk of RbV_3Sb_5 at two temperatures, above and below T_{CO}. The light green curve represents the ab initio prediction in the absence of electronic moments. The dashed black line is obtained by displacing the muon from its equilibrium position by only 0.03 Å, which restores almost perfect agreement with the experimental results. **b** The muon site, indicated by the red ball located between the in-plane Sb1 and the Rb atom in RbV_3Sb_5, was obtained using the DFT +μ method. The figure also shows the displacement of the nearest neighbor Sb atom from the kagome plane formed by V atoms.

for Sb in CsV_3Sb_5, as evidenced by nuclear quadrupole resonance studies[54], nor for Rb in RbV_3Sb_5[55]. This reinforces the conclusion[12] that the observed increase in the relaxation rate at low temperatures is of electronic origin, and that the parameter Γ_{ZF} in Eq. (1) reflects mostly the temperature-dependent electronic contribution. Therefore, an increase in Γ_{ZF} signifies an increase of the local magnetic fields, i.e., the breaking of time-reversal symmetry.

We then examine the depth dependence of the time-reversal symmetry (TRS) breaking signal in both RbV_3Sb_5 and $Cs(V_{0.86}Ta_{0.14})_3Sb_5$ crystals. This is achieved through ZF and low transverse field μSR experiments. For RbV_3Sb_5, the ZF-μSR spectra measured at both the surface ($E = 2$ keV, corresponding to a mean implantation depth, $\bar{z}$, of 10 nm) and in the bulk ($E = 14$ keV, $\bar{z} = 90$ nm) are shown in Fig. 3a. A noticeable difference in the shape of the field distribution was observed between these two depths. Specifically, the ZF-μSR spectrum in the bulk was analyzed using the Eq. 1. Conversely, the ZF-μSR spectrum at the surface is accurately described by only the exponential term. The zero-field relaxation, which is decoupled by applying a small external magnetic field longitudinally aligned with the muon spin polarization ($B_{LF} = 5$ mT, where LF stands for "Longitudinal Field" (see Fig. 3a), suggests that the substantial relaxation observed at the surface is due to spontaneous fields that are static on the

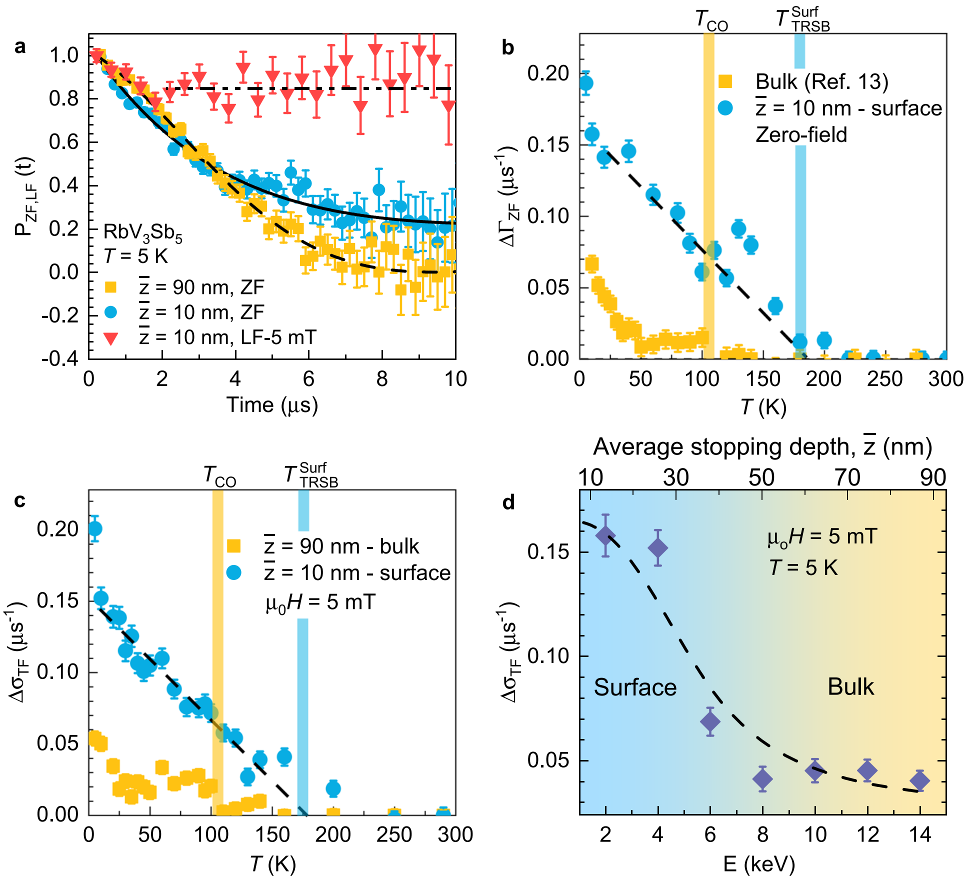

Fig. 3 | Depth dependent magnetism in RbV$_3$Sb$_5$. a The ZF μSR time spectra for the single crystal sample of RbV$_3$Sb$_5$, obtained at T = 5 K at the surface (mean implantation depth of $\bar{z}$ = 10 nm) and in the bulk ($\bar{z}$ = 90 nm). The dashed curve represents a fit to Eq. (1). The solid line represents a fit using only the exponential function $\exp(-\Gamma t)$. The μSR time spectrum, obtained at T = 5 K under the magnetic field of 5mT, applied parallel to the initial muon spin polarization is also shown. The error bars are the standard error of the mean (s.e.m.) in about 10^6 events. **b** Temperature dependence of the relaxation rate $\Delta\Gamma_{ZF} = \Gamma_{ZF}(T) - \Gamma_{ZF}(\mathrm{T{=}300K})$, measured in zero-field, at the surface ($\bar{z} \simeq 10$ nm) and in the bulk ($\bar{z} \simeq 90$ nm) of the single crystal RbV$_3$Sb$_5$. The absolute value of zero-field relaxation rate at room temperature is as follows: $\Gamma_{ZF} \simeq 0.153(5)\ \mu s^{-1}$. **c** Temperature dependence of the relaxation rate $\Delta\sigma_{TF} = \sigma_{TF}(T)$-$\sigma_{TF}(300\mathrm{K})$, measured in an applied field of 5 mT, at the surface ($\bar{z} \simeq 10$ nm) and in the bulk ($\bar{z} \simeq 90$ nm) of the single crystal RbV$_3$Sb$_5$. The error bars represent the standard deviation of the fit parameters. **d** The muon-spin relaxation rate in RbV$_3$Sb$_5$, measured at 5 K and in applied field of 5 mT, as a function of muon implantation energy, E. Top axis shows the average implantation depth, $\bar{z}$. The dashed curve is the predicted behavior of the $\Delta\sigma_{TF}$ assuming a step-like depth dependence and considering the muon implantation profile[59,60].

microsecond timescale[56,57]. The enhancement of the relaxation rate is also observed in weak transverse field (B_{TF} = 5 mT) experiments (transverse-field μSR spectra are shown in the Supplementary Note 2 and the Supplementary Fig. 2). Figure 3b, c depict the temperature dependences of the zero-field and transverse-field relaxation rates, respectively. This is represented in terms of the differences: $\Delta\Gamma_{ZF} = \Gamma_{ZF}(T)$ - $\Gamma_{ZF}(\mathrm{T{=}300K})$ (see Fig. 3b) and $\Delta\sigma_{TF} = \sigma_{TF}(T) - \sigma_{TF}(300\mathrm{K})$ (see Fig. 3c). This approach is adopted to facilitate a clearer comparison between the two sets of data and to remove any potential systematic errors due to the different implantation energies used. The response observed at a depth of 90 nm from the surface is characterized by a two-step increase in the relaxation rate, commencing at the onset of the charge order temperature $T_{CO} \simeq 110$ K. This finding aligns with previous results[13] obtained using the GPS instrument[58], which predominantly probes the bulk response. Previously[13], it was also shown that the two-step behavior becomes more pronounced when a high magnetic field is applied along the c-axis. At a shallower depth of 10 nm, the increase in the relaxation is about four times larger than in the bulk and decreases monotonously with increasing temperature, lacking the two-step feature. Interestingly, this rate tends to plateau at a temperature about 60 K higher than T_{CO} of the bulk. This observation suggests that not only does the magnitude of the magnetic response vary, but also the onset temperature shifts towards higher values at shallower depths. Specifically, the emergence of the TRS breaking signal near the surface occurs at $T^{\mathrm{Surf}}_{\mathrm{TRSB}} \simeq 175$ K. The relaxation rate as a function of implantation energy or mean depth $\bar{z}$, measured under a transverse field of 5 mT and at a temperature of 5 K, is depicted in Fig. 3d. The energy dependence was fitted to the function[59,60]:

$$\Delta\sigma_{TF}(E) = \int_0^\infty P(z,E)\Delta\sigma(z)dz. \tag{2}$$

where $P(z, E)$ is the probability of the muon beam implanted with energy E to stop at a depth z, shown in Fig. 1f. $\Delta\sigma_{TF}$ is assumed to have a step-like function with two regions. This analysis reveals a characteristic depth of $\bar{z}_c \simeq 33$ nm, in which we observe a notable enhancement in the relaxation rate. This finding is significant as it establishes a characteristic depth where the materials properties begin to exhibit marked changes, distinguishing the near surface behavior from that of the bulk.

We now turn our attention to the results for Cs(V$_{0.86}$Ta$_{0.14}$)$_3$Sb$_5$, which are summarized in Fig. 4. Contrary to RbV$_3$Sb$_5$, the variation in the field distribution shape between these two depths is much less pronounced. Figure 4a shows the ZF-μSR spectra measured at both the surface (corresponding to a mean implantation depth, $\bar{z}$, of 10 nm) and

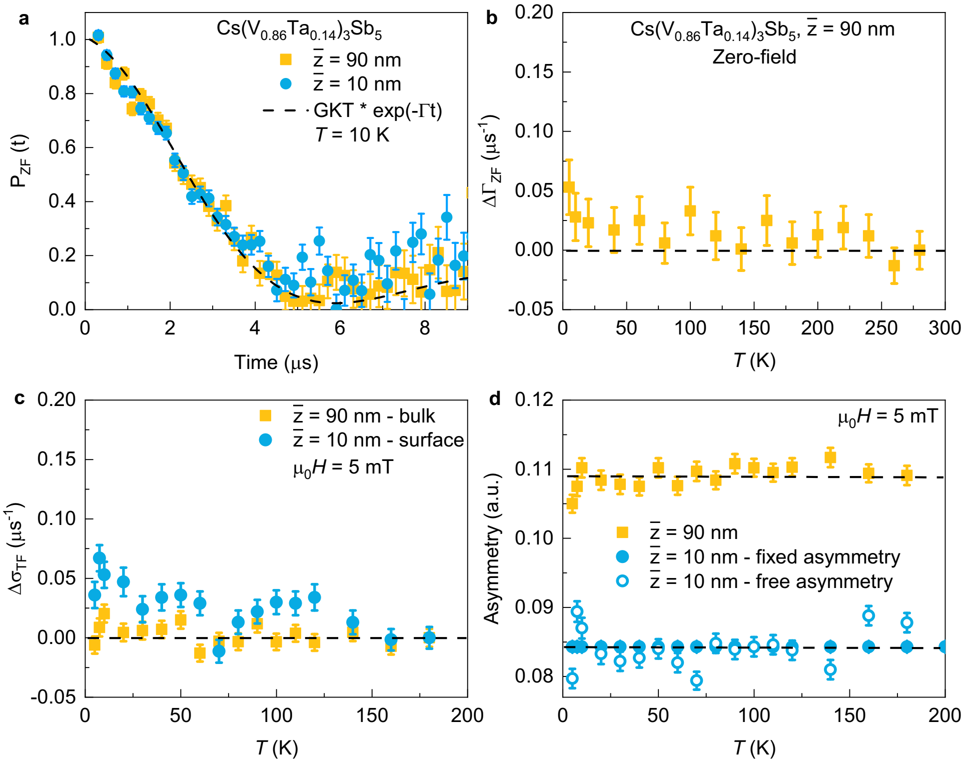

Fig. 4 | Absence of magnetism in $Cs(V_{0.86}Ta_{0.14})_3Sb_5$. **a** The ZF μSR time spectra for the single crystal sample of $Cs(V_{0.86}Ta_{0.14})_3Sb_5$, obtained at $T = 10$ K at the surface (mean implantation depth of $\bar{z} = 10$ nm) and in the bulk ($\bar{z} = 90$ nm). The dashed curve represents a fit to Eq. (1). The error bars are the standard error of the mean (s.e.m.) in about 10^6 events. **b** Temperature dependence of the relaxation rate $\Delta\Gamma_{ZF} = \Gamma_{ZF}(T) - \Gamma_{ZF}(T{=}300K)$, measured in the bulk ($\bar{z} \simeq 90$ nm) of the single crystal $Cs(V_{0.86}Ta_{0.14})_3Sb_5$. **c**, **d** The temperature dependence of the low transverse field (5mT) muon spin relaxation rate $\Delta\sigma_{TF} = \sigma_{TF}(T)$-$\sigma_{TF}(200K)$ (**c**) and the initial asymmetry (**d**), measured at the surface ($\bar{z} \simeq 10$ nm) and in the bulk ($\bar{z} \simeq 90$ nm) of the single crystal $Cs(V_{0.86}Ta_{0.14})_3Sb_5$. The error bars represent the standard deviation of the fit parameters.

in the bulk ($\bar{z} = 90$ nm), indicating a nearly perfect overlap of the field distribution between these two depths. Figure 4b displays the temperature dependence of the zero-field relaxation rate $\Delta\Gamma_{ZF}$, as measured in the bulk at a depth of 90 nm. The rate remains constant across the entire temperature range, with no discernible increase at lower temperatures. These results indicate that in $Cs(V_{0.86}Ta_{0.14})_3Sb_5$, where charge order is fully suppressed, there is an absence of a TRS breaking response. Additionally, as depicted in Fig. 4c, there is no enhancement in the relaxation rate near the surface. This is evident when comparing the transverse field (TF) relaxation rates at depths of $\bar{z} = 90$ nm and $\bar{z} = 10$ nm. The initial asymmetry also exhibits no temperature dependence down to 5K (see Fig. 4d), further confirming the lack of any low-temperature anomalies in $Cs(V_{0.86}Ta_{0.14})_3Sb_5$.

Previous μSR research[12,13,16] uncovered weak internal magnetic fields of around 0.6 G in the charge ordered state of AV_3Sb_5, hinting at spontaneous time-reversal symmetry breaking. However, the faintness of internal fields has often prompted inquiries into their intrinsic nature. In this paper, we report four key findings: (1) Through muon stopping site calculations and local field numerical analysis, we have ruled out muon-induced effects or structural distortions as the cause for the increased zero-field muon spin relaxation rate, attributing it instead to intrinsic magnetism. The observation of TRS-breaking charge order in AV_3Sb_5 has been ascribed to orbital current order within the vanadium kagome layer[18,20,31,32], potentially exerting a significant influence on the superconducting state. Theoretical models indicate an exceedingly small net flux, resulting in a correspondingly minor net magnetic moment within the unit cell of the orbital current order. The hypothesized orbital current is thought to be consistent throughout the lattice, but with an alternating flow direction, leading to non-uniform fields at the muon site. In this context, muons could interact with these closed current loops below the temperature T_{TRSB}^{Surf}, which would result in an enhanced internal field width as detected by the muon ensemble, in the charge ordered state. Similar effects of static magnetic fields appearing near the surface due to orbital loop currents were observed in Sr_2RuO_4 crystals[39]. The muon stopping site in RbV_3Sb_5 is notably distant (~ 3.5 Å) from the vanadium lattice, symmetrically situated around the hexagon of vanadium atoms. This symmetric arrangement, together with the negligible net flux resulting from the orbital currents, can account for the observed small TRS breaking signal in the charge-ordered state. (2) A pronounced enhancement, by a factor of four, of the zero/low-field muon spin relaxation rate is observed near the surface of RbV_3Sb_5 compared to the bulk. The characteristic depth scale at which the enhancement of relaxation occurs is $\bar{d}_c \simeq 33$ nm. Near the surface, i.e., below 33 nm, the estimated field strength is $\Gamma_{12}/\gamma_\mu \simeq 2.5$ G, whereas in the bulk it is 0.6 G. This not only provides stronger evidence of TRS breaking in this material but also demonstrates the significant tunability of the TRS signal under zero-field conditions. (3) Near the surface, the onset of the TRS breaking response seems to occur at a temperature $T_{TRSB}^{Surf} \simeq 175$ K. This indicates that in the bulk of RbV_3Sb_5, TRS breaking takes place within the charge ordered state, whereas near the surface, it emerges at a temperature notably higher than the onset of charge order $T_{CO} \simeq 110$ K. Given that a range of surface and bulk-sensitive methods identify 110 K as the onset temperature for charge order in RbV_3Sb_5, it can be logically inferred that the temperature at which charge order occurs is consistent across both the surface and the bulk. Recent work on the sister compound CsV_3Sb_5 shows that reducing the crystal thickness below 27 nm increases the charge ordering temperature, with a maximum of $T_{CO}^{Surf} \simeq 120$ K (see the Supplementary Note 4 and the Supplementary Fig. 10). However this is still significantly lower than the

$T_{\mathrm{TRSB}}^{\mathrm{Surf}} \simeq 175$ K we found near the surface. (4) Furthermore, in $\mathrm{Cs(V_{0.86}Ta_{0.14})_3Sb_5}$, which lacks charge order, no increase in relaxation rate is observed either at the surface or in the bulk down to 5 K. This strongly suggests a direct correlation between charge order and the TRS breaking signal in $A\mathrm{V_3Sb_5}$ Kagome superconductors and rules out systematic effects as a source of the relaxation enhancement near the surface. These findings also show that while the TRS breaking response is closely related to the presence of charge order, TRS breaking can manifest at temperatures higher than those of charge order onset. In this regard, recent torque measurements[61] have demonstrated a two-fold in-plane magnetic anisotropy above charge order, which breaks the rotational symmetry of the crystal. This finding aligns with our observations.

Our research identifies a kagome superconductor $\mathrm{RbV_3Sb_5}$ as the system with the highest TRS breaking temperature, reaching $\simeq$ 175 K. The observation that the TRS breaking signal at the surface of $\mathrm{RbV_3Sb_5}$ occurs at a higher temperature than the onset of charge order presents an intriguing and novel aspect of the physics in these materials. This suggests that the mechanism driving the TRS breaking phenomenon might be different or more pronounced near the surface. This could mean that surface interactions or reconstructions play a significant role, possibly indicating an enhanced or modified electron correlation effect near the surface compared to the bulk. Typically, it is anticipated that surface effects occur extremely close to the surface. Present investigations suggest that the transition from bulk to surface occurs over a range of 33 nm in $\mathrm{RbV_3Sb_5}$. This observation might open avenues for tuning the electronic properties of these materials through surface engineering, which could be relevant for potential applications in electronic devices where surface properties are crucial. The fact that TRS breaking occurs at a higher temperature than charge order in $\mathrm{RbV_3Sb_5}$ mirrors the behavior observed in cuprate high-temperature superconductors[62], where the pseudogap phase, thought to involve orbital currents[36], also emerges at a higher temperature than charge order. This similarity draws intriguing parallels between these two distinct types of materials and points to potentially fundamental and universal behaviors in these complex material systems.

Methods

Muon-spin rotation

In a μSR (muon spin rotation) experiment, nearly 100% spin-polarized muons μ^+ are implanted into the sample one at a time. These positively charged μ^+ particles thermally stabilize at interstitial lattice sites, effectively serving as magnetic microprobes within the material. In the presence of a magnetic field, the muon spin undergoes precession at the local field B_μ at the muon site, with a Larmor frequency ν_μ given by $\gamma_\mu/(2\pi)B_\mu$, where $\gamma_\mu/(2\pi)$ = 135.5 MHz $\mathrm{T^{-1}}$ represents the muon gyromagnetic ratio.

Experimental details

Zero field (ZF) and weak transverse field (TF) μSR experiments were conducted on single crystalline samples of $\mathrm{RbV_3Sb_5}$ and $\mathrm{Cs(V_{0.86}Ta_{0.14})_3Sb_5}$ using the low energy μSR instrument at the Swiss Muon Source (SμS), Paul Scherrer Institut, in Villigen, Switzerland[46,47]. For these measurements, large single crystal pieces were used. The crystals were carefully arranged in a mosaic layout on a nickel-coated plate and secured with silver epoxy, covering an area of 1.5 × 1.5 $\mathrm{cm^2}$. The samples were mounted on a cold finger cryostat, which accommodates temperatures ranging from 5–300 K. The crystals were aligned such that was done such that the c-axis was parallel to the muon beam and the applied magnetic field. Measurements were carried out with the muon spin polarization both parallel to the c-axis (in a longitudinal configuration) and perpendicular to the c-axis (in a transverse field configuration). We utilized a muon beam that could be adjusted within an energy range of 1 keV to 30 keV. The implantation energy, E, corresponds to a specific muon implantation depth profile, allowing us to vary the implantation depths from a few nanometers to several tens nanometers. This capability facilitated our depth-resolved μSR studies, with approximate depths ranging from $\bar{z}$ = 1–200 nm. In Fig. 3d, we plot our results as a function E (which is the control parameter) and present the corresponding mean depth as a measure of the stopping depth to make the plot more meaningful for the general reader. We also note that the mean depth is almost proportional to E, hence the top axis is scaled accordingly. The muon implantation profiles in $\mathrm{(Rb,Cs)V_3Sb_5}$ for various implantation energies, were simulated using the TrimSP Monte Carlo algorithm[46].

Measurements of both normal and superconducting bulk state properties were conducted using the GPS and the high-field HAL-9500 instruments. HAL-9500 is equipped with a BlueFors vacuum-loaded, cryogen-free dilution refrigerator (DR) for probing the low ttemperature deep bulk properties. At the GPS instrument (πM3) beamline, we utilized a “spin rotator" to alter the muon’s spin orientation. Typically, a muons spin is naturally antiparallel to its momentum, but we rotated it by 45° relative to the c-axis of the crystal. This allowed the samples orientation to remain fixed while the muon spin was adjusted. The rotation angle of 44.5(3)° was precisely determined through measurements in a weak magnetic field, applied transversely to the muon spin polarization.

The μSR data, shown in Fig. 2a, were taken at the ISIS Pulsed Neutron and Muon Source at the Rutherford Appleton Laboratories (UK) using the EMU spectrometer. The powder sample was pressed into a disk of 30 mm in diameter and 1.9 mm in thickness. A 1.25 mm thick Kapton mask was mounted on top of the aluminum sample holder in order to eliminate the background signal originating from muons implanted in the sample holder. It is reasonable to assume that a 1% background is still present in the measurements but, for the sake of simplicity, it is not removed from the experimental asymmetry. Measurements were carried out at 120 K, above the charge ordering transition, and at 5 K, well below T_{CO}. The total asymmetry is determined through transverse field calibration measurements at each temperature, and it is subsequently employed to assess the zero-field total asymmetry. Alternatively, this information can be extracted by fitting the asymmetry with a Kubo-Toyabe function in the interval 0.4 μs to 4μs. The two approaches yield very similar results differing by less than 1%. This procedure allows for the experimental determination of the muon’s spin polarization as a function of time.

ISIS is a pulsed muon source which allows for high data rates. This increases substantially the time window that can be explored and allows to carefully characterize the tail of the polarization function. At the same time, the muon beam spot size is much larger than at PSI thus precluding single crystal measurements for these materials.

Analysis of transverse field μSR data

Muon spin rotation data were processed utilizing the software Musrfit, which was developed at the Paul Scherrer Institute[63]. The TF-μSR data were analyzed by using the following functional form[63]:

$$A_{TF}(t) = A_S e^{\left[-\frac{\sigma_{TF}^2 t^2}{2}\right]} \cos(\gamma_\mu B_{\mathrm{int}} t + \varphi), \tag{3}$$

Here A_S denotes the initial assymmetry, and φ is the initial phase of the muon-spin ensemble. B_{int} represents the internal magnetic field at the muon site, and the relaxation rate σ_{TF} characterize the damping of the μSR signal.

Computational details

The muon sites in $\mathrm{RbV_3Sb_5}$ have been investigated with Density Functional Theory (DFT) using the so called DFT+μ[50] approach. The tri-hexagonal lattice structure[64,65] was used to perform all simulations unless otherwise specified. This structure has *Fmmm* symmetry with lattice parameters set to 10.943, 18.954 and 18.146 Å for *a*, *b* and *c*, respectively[66]. The simulations were carried out using the plane wave based code QuantumESPRESSO v7.1[67] The structural relaxation of all lattice structures was performed with GBRV ultrasoft pseudopotentials[68] using 40 Ry cutoff for the planewave expansion of wavefunctions and 320 Ry cutoff for the charge density. The PBEsol[69] functional was used to estimate the exchange and correlation term. The reciprocal space was sampled with the Gamma point. The optimization of atomic coordinates was carried out until forces and total energy differences were less than 0.5 mRy/Bohr and 0.09 mRy respectively. In order to find the stable muon sites we sampled the interstitial space of the host lattice using a grid with 1.2 Å spacing between the points and removed all symmetry equivalent positions as well as all points closer than 1.3 Å to the atoms of RbV_3Sb_5. This results in 71 starting interstitial positions. After structural relaxations, 34 symmetrically inequivalent positions are found using the clustering algorithm available in ref. 70. For the stable muon sites a refined equilibrium position and the Electric Field Gradients (EFG) at the nuclei of the lattice, obtained with the GIPAW code[71], are estimated with a 2 × 1 × 1 supercell.

Data availability

All relevant data are available from the authors. Alternatively, the computational results can be accessed through the link https://doi.org/10.24435/materialscloud:4f-r5 and muon-spin rotation data can be accessed through the data base at the following link http://musruser.psi.ch/cgi-bin/SearchDB.cgi using the following details: 1. Area: LEM. Year: 2022. Run Title: RbV_3Sb_5 xtals... Run from 0700 to 0770 and from from 1411 to 1434. 2. Area: LEM. Year: 2022. Run Title: $CsV_{3-x}Ta_xSb_5$.... Run from 5475 to 5567.

References

1. Syôzi, I. Statistics of Kagome Lattice. *Prog. Theor. Phys.* **6**, 306 (1951).
2. Zhou, Y., Kanoda, K. & Ng, T.-K. Quantum spin liquid states. *Rev. Mod. Phys.* **89**, 025003 (2017).
3. Yin, J.-X. Giant and anisotropic spin-orbit tunability in a strongly correlated kagome magnet. *Nature* **562**, 91–95 (2018).
4. Ye, L. Massive Dirac fermions in a ferromagnetic kagome metal. *Nature* **555**, 638–642 (2018).
5. Guguchia, Z. et al. Tunable anomalous Hall conductivity through volume-wise magnetic competition in a topological kagome magnet. *Nat. Commun.* **11**, 559 (2020).
6. Ghimire, N. J. & Mazin, I. I. Topology and correlations on the kagome lattice. *Nat. Mater.* **19**, 137–138 (2020).
7. Ortiz, B. et al. CsV_3Sb_5: A Z_2 Topological Kagome Metal with a Superconducting Ground State. *Phys. Rev. Lett.* **125**, 247002 (2020).
8. Ortiz, B. et al. Superconductivity in the Z_2 kagome metal KV_3Sb_5. *Phys. Rev. Mater.* **5**, 034801 (2021).
9. Yin, Q. et al. Superconductivity and normal-state properties of kagome metal RbV_3Sb_5 single crystals. *Chin. Phys. Lett.* **38**, 037403 (2021).
10. Wilson, S.D. and Ortiz, B.R. AV_3Sb_5 Kagome Superconductors: Progress and Future Directions. arXiv:2311.05946 (2023).
11. Jiang, Y.-X. et al. Discovery of topological charge order in kagome superconductor KV_3Sb_5. *Nat. Mater.* **20**, 1353–1357 (2021).
12. Mielke III, C. et al. Time-reversal symmetry-breaking charge order in a kagome superconductor. *Nature* **602**, 245–250 (2022).
13. Guguchia, Z. et al. Tunable unconventional kagome superconductivity in charge ordered RbV_3Sb_5 and KV_3Sb_5. *Nat. Commun.* **14**, 153 (2023).
14. Guguchia, Z. et al. Hidden magnetism uncovered in a charge ordered bilayer kagome material ScV_6Sn_6. *Nat. Commun.* **14**, 7796 (2023).
15. Guguchia, Z., Khasanov, R. & Luetkens, H. Unconventional charge order and superconductivity in kagome-lattice systems as seen by muon-spin rotation. *npj Quantum Mater.* **8**, 41 (2023).
16. Khasanov, R. et al. Time-reversal symmetry broken by charge order in CsV_3Sb_5. *Phys. Rev. Res.* **4**, 023244 (2022).
17. Neupert, T., Denner, M. M., Yin, J.-X., Thomale, R. & Hasan, M. Z. Charge order and superconductivity in kagome materials. *Nat. Phys.* **18**, 137–143 (2022).
18. Denner, M., Thomale, R. & Neupert, T. Analysis of charge order in the kagome metal AV_3Sb_5 (A = K, Rb, Cs). *Phys. Rev. Lett.* **127**, 217601 (2021).
19. Zhong, Y. et al. Nodeless electron pairing in CsV_3Sb_5-derived kagome superconductors. *Nature* **617**, 488–492 (2023).
20. Christensen, M. H., Birol, T., Andersen, B. M. & Fernandes, R. M. Loop currents in AV_3Sb_5 kagome metals: multipolar and toroidal magnetic orders. *Phys. Rev. B* **106**, 144504 (2022).
21. Wagner, G., Guo, C., Moll, P. J., Neupert, T. & Fischer, M. H. Phenomenology of bond and flux orders in kagome metals. *Phys. Rev. B* **108**, 125136 (2023).
22. Grandi, F. et al. Theory of nematic charge orders in kagome metals. *Phys. Rev. B* **107**, 155131 (2023).
23. Guo, C. et al. Switchable chiral transport in charge-ordered kagome metal CsV_3Sb_5. *Nature* **611**, 461–466 (2022).
24. Yang, S. Giant, unconventional anomalous Hall effect in the metallic frustrated magnet candidate, KV_3Sb_5. *Sci. Adv.* **6**, 1–7s (2020).
25. Yu, F. Concurrence of anomalous Hall effect and charge density wave in a superconducting topological kagome metal. *Phys. Rev. B* **104**, 041103 (2021).
26. Zhao, H. et al. Cascade of correlated electron states in the kagome superconductor CsV_3Sb_5. *Nature* **599**, 216–221 (2021).
27. Chen, H. et al. Roton pair density wave in a strong-coupling kagome superconductor. *Nature* **599**, 222–228 (2021).
28. Nie, L. et al. Charge-density-wave-driven electronic nematicity in a kagome superconductor. *Nature* **604**, 59–64 (2022).
29. Yu, L. et al. Evidence of a hidden flux phase in the topological kagome metal CsV_3Sb_5. arXiv:2107.10714 (2021).
30. Xu, Y. et al. Three-state nematicity and magneto-optical Kerr effect in the charge density waves in kagome superconductors. *Nat. Phys.* **18**, 1470–1475 (2022).
31. Park, T., Ye, M. & Balents, L. Electronic instabilities of kagome metals: Saddle points and Landau theory. *Phys. Rev. B* **104**, 035142 (2021).
32. Lin, Y.-P. & Nandkishore, R. M. Complex charge density waves at Van Hove singularity on hexagonal lattices: Haldane-model phase diagram and potential realization in the kagome metals AV_3Sb_5. *Phys. Rev. B* **104**, 045122 (2021).
33. Chandan Setty, C., Hu, H., Chen, L., Si, Q. Electron correlations and T-breaking density wave order in a Z_2 kagome metal, https://arxiv.org/abs/2105.15204 (2021).
34. Guo, C. et al. Correlated order at the tipping point in the kagome metal CsV_3Sb_5. *Nat. Phys.* **20**, 579–584 (2024).
35. Haldane, F. D. M. Model for a quantum Hall effect without Landau levels: condensed-matter realization of the parity anomaly. *Phys. Rev. Lett.* **61**, 2015–2018 (1988).
36. Varma, C. M. Non-Fermi-liquid states and pairing instability of a general model of copper oxide metals. *Phys. Rev. B* **55**, 14554–14580 (1997).
37. Luke, G. M. et al. Time-reversal symmetry-breaking superconductivity in Sr_2RuO_4. *Nature* **394**, 559 (1998).
38. Hillier, A. D., Jorge, Q. & Cywinski, R. Evidence for Time-Reversal Symmetry Breaking in the Noncentrosymmetric Superconductor $LaNiC_2$. *Phys. Rev. Lett.* **102**, 117007 (2009).
39. Fittipaldi, R. et al. Unveiling unconventional magnetism at the surface of Sr_2RuO_4. *Nat. Commun.* **12**, 5792 (2021).

40. Shan, Z. et al. Muon spin relaxation study of the layered kagome superconductor CsV$_3$Sb$_5$. *Phys. Rev. Res.* **4**, 033145 (2022).
41. Shumiya, N. et al. Tunable chiral charge order in kagome superconductor RbV$_3$Sb$_5$. *Phys. Rev. B* **104**, 035131 (2021).
42. Wang, Z. et al. Electronic nature of chiral charge order in the kagome superconductor CsV$_3$Sb$_5$. *Phys. Rev. B* **104**, 075148 (2021).
43. Xing, Y. et al. Optical Manipulation of the Charge Density Wave state in RbV$_3$Sb$_5$. *Nature* **631**, 60–66 (2024).
44. Saykin, D. R. et al. High Resolution Polar Kerr Effect Studies of CsV$_3$Sb$_5$: Tests for Time-Reversal Symmetry Breaking below the Charge-Order Transition. *Phys. Rev. Lett.* **131**, 016901 (2023).
45. Song, B. et al. Anomalous enhancement of charge density wave in kagome superconductor CsV$_3$Sb$_5$ approaching the 2D limit. *Nat. Commun.* **14**, 2492 (2023).
46. Morenzoni, E. et al. Implantation studies of keV positive muons in thin metallic layers. *Nucl. Instrum. Methods Phys. Res. Sect. B* **192**, 254–266 (2002).
47. Prokscha, T. et al. The new μE4 beam at PSI: a hybrid-type large acceptance channel for the generation of a high intensity surface-muon beam. *Nucl. Instrum. Methods Phys. Res. A* **595**, 317–331 (2008).
48. Bonfà, P. Entanglement between Muon and $I > 1/2$ Nuclear Spins as a Probe of Charge Environment. *Phys. Rev. Lett.* **129**, 097205 (2022).
49. Kubo, R. & Toyabe, T. Magnetic Resonance and Relaxation *North Holland*, Amsterdam, (1967).
50. Blundell, S. J. & Lancaster, T. DFT+μ: Density functional theory for muon site determination. *Appl. Phys. Rev.* **10**, 021316 (2023).
51. Celio, M. New Method to Calculate the Muon Polarization Function. *Phys. Rev. Lett.* **56**, 2720 (1986).
52. Bonfà, P., Frassineti, J., Isah, M. M., Onuorah, I. J. & Sanna, S. UNDI: An open-source library to simulate muon-nuclear interactions in solids. *Computer Phys. Commun.* **260**, 107719 (2021).
53. Moller, J. S., Ceresoli, D., Lancaster, T., Marzari, N. & Blundell, S. J. Quantum states of muons in fluorides. *Phys. Rev. B* **87**, 121108 (2013).
54. Feng, X. Y. Commensurate-to-incommensurate transition of charge-density-wave order and a possible quantum critical point in pressurized kagome metal CsV$_3$Sb$_5$. *npj Quantum Mater.* **8**, 23 (2023).
55. Frassineti, J. Study of charge, spin, and structural orderings in quantum materials using nuclei and muons as local probes. Ph.D. thesis, Dottorato di Ricerca in Fisica, Alma Mater Studiorum - Universita di Bologna (2024).
56. Amato, A. Physics with Muons: from Atomic Physics to Condensed Matter Physics. https://www.psi.ch/en/lmu/lectures (22.03.2020).
57. Dalmas de Reotier, P. & Yaouanc, A. Muon spin rotation and relaxation in magnetic materials. *J. Phys. Condens. Matter* **9**, 9113 (1997).
58. Amato, A. et al. The new versatile general purpose surface-muon instrument (GPS) based on silicon photomultipliers for μSR measurements on a continuous-wave beam. *Rev. Sci. Instrum.* **88**, 093301 (2017).
59. Martins, M. M. et al. Depth profiling of LE-μSR parameters with musrfit. *J. Phys.: Conf. Ser.* **2462**, 012025 (2023).
60. Simões, A. F. A. et al. Muon implantation experiments in films: Obtaining depth-resolved information. *Rev. Sci. Instrum.* **91**, 023906 (2020).
61. Asaba, T. et al. Evidence for an odd-parity nematic phase above the charge-density-wave transition in a kagome metal. *Nat. Phys.* **20**, 40–46 (2024).
62. Keimer, B., Kivelson, S. A., Norman, M. R., Uchida, S. & Zaanen, J. From quantum matter to high-temperature superconductivity in copper oxide. *Nature* **518**, 179 (2015).
63. Suter, A. & Wojek, B. M. Musrfit: a free platform-independent framework for μ SR data analysis. *Phys. Procedia* **30**, 69 (2012).
64. Miao, H. et al. Geometry of the charge density wave in the kagome metal AV 3 Sb 5. *Phys. Rev. B* **104**, 195132 (2021).
65. Tan, H., Liu, Y., Wang, Z. & Yan, B. Charge density waves and electronic properties of superconducting kagome metals. *Phys. Rev. Lett.* **127**, 046401 (2021).
66. Ortiz, B. R. et al. New kagome prototype materials: discovery of KV 3 Sb 5, RbV 3 Sb 5, and CsV 3 Sb 5. *Phys. Rev. Mater.* **3**, 094407 (2019).
67. Giannozzi, P. et al. QUANTUM ESPRESSO: a modular and open-source software project for quantum simulations of materials. *J. Phys.: Condens. Matter* **21**, 395502 (2009).
68. Garrity, K. F., Bennett, J. W., Rabe, K. M. & Vanderbilt, D. Pseudopotentials for high-throughput DFT calculations. *Comput. Mater. Sci.* **81**, 446–452 (2014).
69. Perdew, J. P. et al. *Phys. Rev. Lett.***100**, 136406 (2008).
70. Onuorah, I., Bonacci, M., Pizzi, G. & Bonfa, P. aiida-muon, https://arxiv.org/abs/2408.16722v1 (2023).
71. Ceresoli, D. et al. GIPAW, Software, available at: https://github.com/dceresoli/qe-gipaw (2024).

Acknowledgements

The μSR experiments were carried out at the Swiss Muon Source (SμS) Paul Scherrer Institute, Villigen, Switzerland. Some of the data were also collected at the ISIS facility, STFC Rutherford Appleton Laboratory, UK. Authors acknowledge Peter Baker and Rhea Stewart for technical support and fruitful discussions. Z.G. acknowledges support from the Swiss National Science Foundation (SNSF) through SNSF Starting Grant (No. TMSGI2_211750). S.D.W. and A.C.S. gratefully acknowledge support via the UC Santa Barbara NSF Quantum Foundry funded via the Q-AMASE-i program under award DMR-1906325. M.Z.H. is supported by U.S. DOE under the Basic Energy Sciences Grant No. DOE/BES DE-FG-02-05ER46200. P.B. acknowledges financial support from PNRR MUR project ECS_00000033_ECOSISTER. We also gratefully acknowledge the use of the computing resources provided by STFC Scientific Computing Department's SCARF cluster.

Author contributions

Z.G. conceived and supervised the project. Growth of the single crystals RbV$_3$Sb$_5$ and Cs(V$_{0.86}$Ta$_{0.14}$)$_3$Sb$_5$: Y.Z., K.O., S.W., A.C.S. AND Z.W. Low energy muon spin rotation experiments, analysis and corresponding discussions: J.N.G, C.M.III, D.D., M.M., V.S., M.F., T.T., J.-X.Y., M.Z.H., H.L., R.K., S.S., P.B., A.S., T.P., Z.S., and Z.G. Muon stopping site calculations, local field numerical analysis and corresponding discussions: T.M., S.S., Z.G., and P.B. Figure development and writing of the paper: Z.G. with contributions from P.B., J.N.G and other authors. All authors discussed the results, interpretation and conclusion.

Competing interests

All authors declare that they have no competing interests.

Additional information

Supplementary information The online version contains supplementary material available at https://doi.org/10.1038/s41467-024-52688-6.

Correspondence and requests for materials should be addressed to P. Bonfà or Z. Guguchia.

Peer review information *Nature Communications* thanks the anonymous reviewers for their contribution to the peer review of this work. A peer review file is available.

Reprints and permissions information is available at http://www.nature.com/reprints